

# COSMOGLOBE DR2. VII. Towards a concordance model of large-scale thermal dust emission for microwave and infrared frequencies

E. Gjerløw<sup>1\*</sup>, R. M. Sullivan<sup>1</sup>, R. Aurvik<sup>1</sup>, A. Basyrav<sup>1</sup>, L. A. Bianchi<sup>1</sup>, A. Bonato<sup>2</sup>, M. Brilenkov<sup>1</sup>, H. K. Eriksen<sup>1</sup>, U. Fuskeland<sup>1</sup>, M. Galloway<sup>1</sup>, K. A. Glasscock<sup>1</sup>, L. T. Hergt<sup>3</sup>, D. Herman<sup>1</sup>, J. G. S. Lunde<sup>1</sup>, A. I. Silva Martins<sup>1</sup>, M. San<sup>1</sup>, D. Sponseller<sup>4</sup>, N.-O. Stutzer<sup>1</sup>, H. Thommesen<sup>1</sup>, V. Vikenes<sup>1</sup>, D. J. Watts<sup>1</sup>, I. K. Wehus<sup>1</sup>, and L. Zapelli<sup>2,5,6</sup>

<sup>1</sup> Institute of Theoretical Astrophysics, University of Oslo, Blindern, Oslo, Norway

<sup>2</sup> Dipartimento di Fisica, Università degli Studi di Milano, Via Celoria, 16, Milano, Italy

<sup>3</sup> Department of Physics and Astronomy, University of British Columbia, 6224 Agricultural Road, Vancouver BC, V6T1Z1, Canada

<sup>4</sup> Department of Space, Earth and Environment, Chalmers University of Technology, Gothenburg, Sweden

<sup>5</sup> Università di Trento, Università degli Studi di Milano, CUP E66E23000110001

<sup>6</sup> INFN sezione di Milano, 20133 Milano, Italy

January 12, 2026

## ABSTRACT

We fit a four-component thermal dust model to *COBE*-DIRBE data between 3.5 and 240  $\mu\text{m}$  within the global Bayesian end-to-end COSMOGLOBE DR2 reanalysis. Following a companion analysis of *Planck* HFI, the four components of this model correspond to “hot dust”, “cold dust”, “nearby dust”, and “H $\alpha$  correlated dust”, respectively, and each component is modelled in terms of a fixed spatial template and a spatially isotropic spectral energy density (SED) defined by an overall free amplitude for each DIRBE channel. The H $\alpha$  dust is an extinction component and, as such, has a negative amplitude. Except for the cold dust amplitude, which is only robustly detected in the 240  $\mu\text{m}$  channel, we measure statistically significant template amplitudes for all components in all DIRBE channels between 3.5 and 240  $\mu\text{m}$ . However, the two highest frequency channels are too dominated by starlight emission to allow robust dust detections. The total number of DIRBE-specific degrees of freedom in this model is thus only 25. Despite this low dimensionality, the resulting total SED agrees well with recent astrodust predictions, and the overall model efficiency is high although with a notable wavelength dependency. At both low and high frequencies, more than 95 % of the signal root mean squared is captured by the model, while at 60 and 100  $\mu\text{m}$  about 70 % of the signal is successfully accounted for. The hot dust component, which was previously found to correlate strongly with C II emission, has the highest absolute amplitude in all DIRBE frequency channels; at 3.5  $\mu\text{m}$ , which is known to be dominated by polycyclic aromatic hydrocarbon emission, this component accounts for at least 80 % of the total signal. This analysis represents an important step towards establishing a joint concordance model of thermal dust emission applicable to both the microwave and infrared regimes, and we conclude by outlining a roadmap to a future joint analysis of AKARI, DIRBE, IRAS, and *Planck*.

**Key words.** ISM: general - Zodiacal dust, Interplanetary medium - Cosmology: observations, diffuse radiation - Galaxy: general

## Contents

### 1. Introduction

In a series of seven companion papers, within which this is the last, we have reanalyzed the 30-year old *COBE*-DIRBE data using modern end-to-end Bayesian statistical techniques as implemented in the COSMOGLOBE<sup>1</sup> framework. From this work, a set of 10 full-sky DIRBE frequency maps emerge, presented in ?, covering the infrared frequency range between 1.25 and 240  $\mu\text{m}$ . These maps have both substantially lower systematic errors and better error characterization compared to their official counterparts (?), and, in particular, they suffer far less from zodiacal light contamination (?). As a result they can be used for more detailed astrophysics applications. A few examples of this are presented in the current analysis, including improved estimates of the cosmic infrared background spectrum (?) and large-scale starlight emission ?.

The main topic of the last three papers in the series is modelling thermal dust radiation efficiently on large angular scales in the microwave and infrared frequency regimes. This issue has been the focus of intense scrutiny ever since the groundbreaking IRAS measurements were published in 1982, and its scientific importance has only increased through the release of a series of increasingly sensitive data sets, such as *COBE*-DIRBE and *Planck* HFI. Today, detailed dust modelling plays a key role in many of the most competitive fields of cosmology, from the search for inflationary gravitational waves in cosmic microwave background (CMB) *B*-mode polarization data (?) to measurements of dark energy using distant supernovae (?).

As of today, *Planck* HFI defines the state-of-the-art for full-sky thermal dust mapping, both in terms of signal-to-noise ratio as well as systematic control. Based on *Planck*'s nine frequency channels, the team produced several exquisite dust models in both intensity and polarization (???????), and these now form the basis for much of the dust modelling efforts in the field (e.g., ??). However, at the same time, the limited frequency range of *Planck*, covering only 30–857 GHz, implies that the applicability of these models are currently quite limited. Furthermore, the absolute calibration of the 857 GHz *Planck* channel, which is nom-

\* Corresponding author: E. Gjerløw; [eirik.gjerlow@astro.uio.no](mailto:eirik.gjerlow@astro.uio.no)

<sup>1</sup> <http://cosmoglobe.uio.no>

inally the most sensitive *Planck* dust channel, is uncertain at the  $\sim 10\%$  level (??), and this induces a large uncertainty on the dust spectral energy density (SED) parameters when extrapolating to higher frequencies.

In the current paper, we address these issues by fitting the multi-component dust model proposed by ? and ? to the re-processed *COBE*-DIRBE data within the COSMOGLOBE DR2 analysis framework. This model consists of four primary components: 1) cold dust, 2) hot dust, 3) nearby dust, and 4)  $H\alpha$ -correlated dust (observed in extinction). From the previous papers, this model is already known to fit the *Planck* HFI frequencies very well when coupled to simple modified blackbody (MBB) SEDs with spatially constant spectral parameters, and in this paper we show that the same spatial morphologies also trace dust in the DIRBE frequencies very well, although with more complicated SED behaviour. The combined result is an global model that jointly describes both microwave and infrared frequencies.

So far, this model has only been developed for and applied to intensity measurements. However, polarized thermal dust emission also plays a key role in modern astrophysics and cosmology. For instance, massive resources are currently being spent on searching for and constraining the amplitude of inflationary gravitational waves through deep CMB  $B$ -mode polarization experiments (??), and polarized thermal dust emission represents a key challenge for these. Given the high efficiency of the COSMOGLOBE DR2 four-component dust model for intensity data, it is reasonable to expect a similar performance for polarization observations. We therefore conclude this paper by outlining one potential roadmap towards a future concordance model for thermal dust emission in both intensity and polarization.

## 2. Bayesian modelling of thermal dust emission in COSMOGLOBE DR2

This paper, being a part of the second COSMOGLOBE Data Release (DR2), is a global, Bayesian analysis mapping out the joint posterior of all involved parameters, and thus intricately bound up with the other papers in the release, both in terms of the data sets and data model used. Hence, here we will here recap of the data model used, as presented in (?), after which we will devote a subsection to how the thermal dust part of the global model is described.

### 2.1. Data model and posterior distribution

In the COSMOGLOBE framework, the standard modus operandi is to begin with an explicit parametric model incorporating all known aspects of the dataset with which we are working – including both instrumental effects as well as a physical model of what is being observed. The DIRBE time-ordered data (TOD) used in this analysis have been parametrized thus:

$$\begin{aligned} \mathbf{d}_{\text{DIRBE}}(\nu) &= \mathbf{GP} \left[ \mathbf{B} \sum_{c=1}^{n_{\text{comp}}} \mathbf{M}_c(\nu) \mathbf{a}_c + \mathbf{s}_{\text{zodi}}(\nu) + \mathbf{s}_{\text{static}}(\nu) \right] + \mathbf{n} \\ &\equiv \mathbf{s}^{\text{tot}} + \mathbf{n}, \end{aligned} \quad (1)$$

where  $\nu$  is the frequency at which we observe,  $\mathbf{d}$  is the stacked TODs,  $\mathbf{G}$  is an overall gain factor,  $\mathbf{P}$  is the pointing matrix which projects the pixelated sky onto a  $n_{\text{tod}}$ -sized space,  $\mathbf{B}$  is the instrumental beam convolution operator, and  $\mathbf{n}$  is the instrumental noise. The physical sky is represented by three terms. Firstly, a

sum over sky components that can be modelled as constant at every point in time. We sum HEALPix<sup>2</sup> (??) maps of amplitudes for each sky component ( $\mathbf{a}_c$ ) multiplied by a mixing matrix  $\mathbf{M}_c$  which extrapolates the given component to the frequencies observed. Secondly, there is a term representing the zodiacal emission, which cannot be treated as a time constant. Finally there is a term representing a component that is static in solar coordinates, which may either be related to the DIRBE sidelobes, or be genuine excess radiation originating in the Solar System. These two last terms are treated in ? and ?, and what concerns us in the present work is the first of the three terms, which will be expanded on in what follows.

### 2.1.1. Bayesian end-to-end analysis

In this analysis, we draw samples from the *posterior* distribution of the full set of parameters of our model (?) – in formulaic terms, we are mapping out  $P(\theta|\mathbf{d})$ , the probability distribution of the set of parameters  $\theta$  given the observed data  $\mathbf{d}$ . Bayes' theorem allows us to write that

$$P(\theta|\mathbf{d}) = \frac{P(\mathbf{d}|\theta)P(\theta)}{P(\mathbf{d})}, \quad (2)$$

and, since  $P(\mathbf{d})$  typically only enters as a normalizing term, as long as the parameter space does not change, sampling from  $P(\theta|\mathbf{d})$  is (modulo a prior term) equivalent to sampling from  $P(\mathbf{d}|\theta) \equiv \mathcal{L}(\theta)$ , the so-called *likelihood* function.

The number of parameters involved in our model (Eq. ??) is of the order of millions, making sampling from the likelihood function a non-trivial task. The COSMOGLOBE framework is based on the Commander software (??), which maps out the posterior parameter distribution through a process called *Gibbs sampling* (e.g., ?), a Monte-Carlo method based on sequentially sampling each parameter (or a subset of parameters) from their respective marginal distributions with respect to all other parameters. The theory of Gibbs sampling then says that by combining these samples into a full set for all the parameters involved, this set will represent a proper sample from the joint distribution. Applied to Eq. ??, we get a sequence of operations as follows:

$$\begin{aligned} \mathbf{G} &\leftarrow P(\mathbf{G} \mid \mathbf{d}, \xi_n, \beta_{\text{sky}}, \mathbf{a}_{\text{sky}}, \zeta_z, \mathbf{a}_{\text{static}}) \\ \xi_n &\leftarrow P(\xi_n \mid \mathbf{d}, \mathbf{G}, \beta_{\text{sky}}, \mathbf{a}_{\text{sky}}, \zeta_z, \mathbf{a}_{\text{static}}) \\ \beta_{\text{sky}} &\leftarrow P(\beta_{\text{sky}} \mid \mathbf{d}, \mathbf{G}, \xi_n, \mathbf{a}_{\text{sky}}, \zeta_z, \mathbf{a}_{\text{static}}) \\ \mathbf{a}_{\text{sky}} &\leftarrow P(\mathbf{a}_{\text{sky}} \mid \mathbf{d}, \mathbf{G}, \xi_n, \beta_{\text{sky}}, \zeta_z, \mathbf{a}_{\text{static}}) \\ \zeta_z &\leftarrow P(\zeta_z \mid \mathbf{d}, \mathbf{G}, \xi_n, \beta_{\text{sky}}, \mathbf{a}_{\text{sky}}, \mathbf{a}_{\text{static}}) \\ \mathbf{a}_{\text{static}} &\leftarrow P(\mathbf{a}_{\text{static}} \mid \mathbf{d}, \mathbf{G}, \xi_n, \beta_{\text{sky}}, \mathbf{a}_{\text{sky}}, \zeta_z) \end{aligned} \quad (3)$$

Here, the symbol  $\leftarrow$  indicates the operation of drawing a sample from the distribution on the right-hand side. After some burn-in period, the resulting joint parameter sets will correspond to samples drawn from the true underlying joint posterior.

Since every step of the Gibbs sampling process assumes that all other parameters are “given”, we can now treat a highly interconnected problem (i.e. sampling from the joint posterior of all parameters involved in our data model) as a highly modular one – meaning that we can perform each “sub-analysis” without being concerned with the other parts of the problem. Hence, in this paper, we mainly focus on the three first components of Eq. ??, leaving the treatment of stars to ?, monopoles to ?, and condition on free-free emission as determined by ?.

<sup>2</sup> <http://healpix.sourceforge.net/>

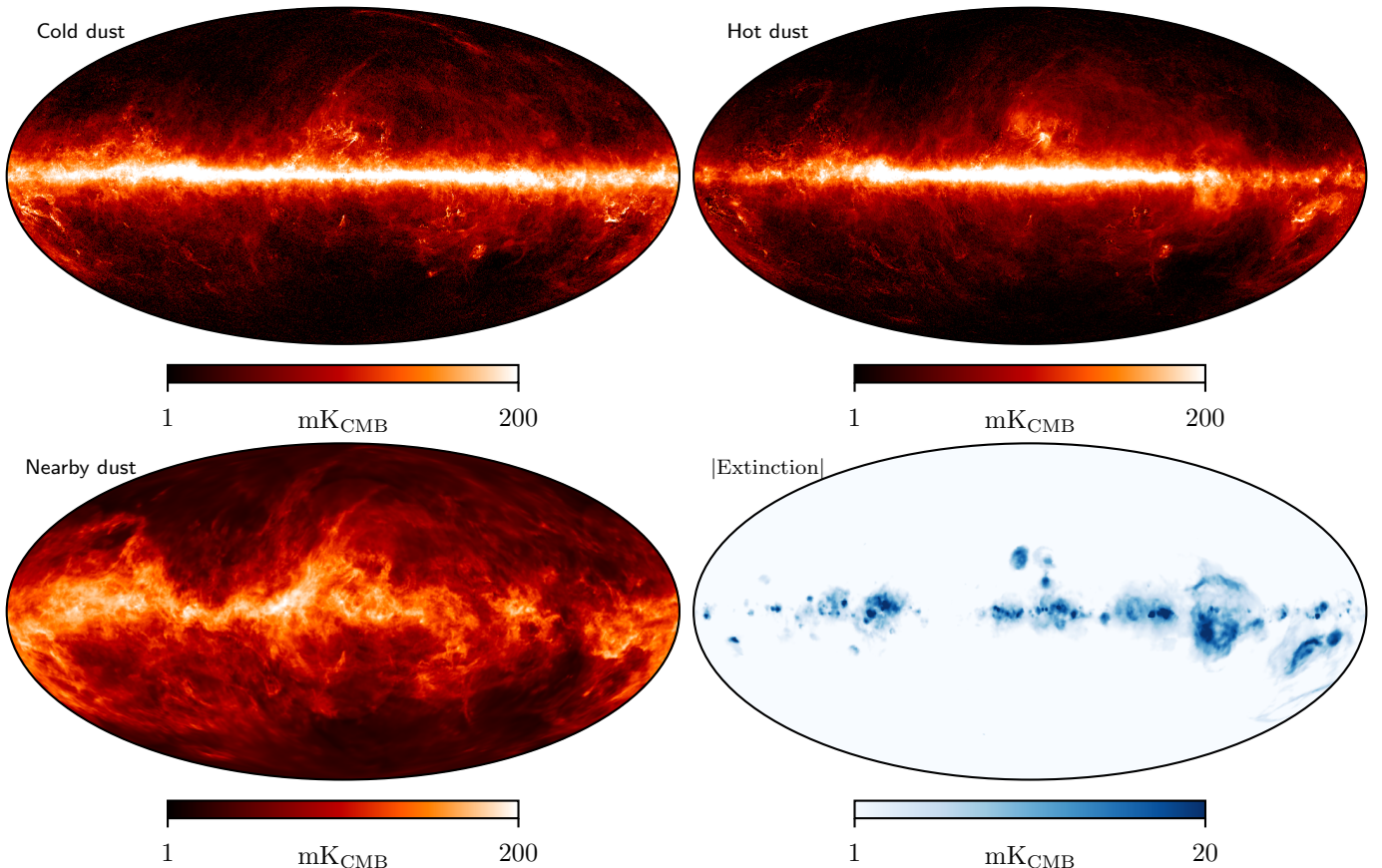


**Fig. 1.** Dust amplitude maps used in the COSMOGLobe DR2 sky model, as evaluated for the *Planck* HFI 545-1 bolometer channel. From left to right and top to bottom, the four panels show 1) the cold dust amplitude,  $a_{\text{cold}}$ ; 2) the hot dust amplitude,  $a_{\text{hot}}$ ; 3) the nearby dust amplitude,  $a_{\text{near}}$ ; and 4) the (absolute value of the) H $\alpha$ -correlated dust extinction amplitude,  $a_{\text{H}\alpha}$ . All panels employ the *Planck* non-linear high dynamic range color scheme, defined by  $\log_{10}((a + \sqrt{4 + a^2})/2)$ , which results in a nearly linear behaviour for small values and exponential for large values.

## 2.2. Multi-component thermal dust modelling

Interstellar dust – amorphous particles of silicate and carbonaceous materials – makes its presence known on practically all astrophysically relevant wavelengths. The efforts to classify and describe this material is significant in its own right, but knowing its properties is critical for better and more precise astrophysical foreground removal in cases where interstellar dust emission contaminate the other signals of interest<sup>3</sup>.

Recently, the “astrodust+PAH” model (?) was introduced, wherein the diffuse interstellar medium (ISM) is hypothesised to be made up of a single composite material (the eponymous astrodust) for scales larger than  $\sim 0.02 \mu\text{m}$ , and a distinct variety of materials – including so-called polycyclic aromatic hydrocarbons (PAH) – on scales smaller than this.

In the wavelength regime between  $3000 - 100 \mu\text{m}$ , this model is described well by an MBB SED<sup>4</sup>, i.e., an SED that follows

$$s(\nu) \propto \nu^\beta B(\nu, T), \quad (4)$$

where  $\nu$  is frequency,  $B$  is the Planck law for a perfect blackbody at a certain frequency  $\nu$  and temperature  $T$ , and  $\beta$  is the spectral index. Typical temperatures of this blackbody in the diffuse ISM are around  $\sim 20 \text{ K}$ , meaning that the distribution typically peaks around  $150 \mu\text{m}$  ( $\sim 2000 \text{ GHz}$ ).

<sup>3</sup> For a recent review, see ?.

<sup>4</sup> The actual astrodust model is made up of a composite MBB which has a transition between 353 and 217 GHz

At lower wavelengths ( $2.5 \mu\text{m} - 12 \mu\text{m}$ ), the astrodust+PAH model is mostly dominated by the nanoscale particle emission, and exhibits strong emission lines at various wavelengths (see Fig. 10 in ?).

### 2.2.1. The four-component dust model

The astrodust model provides a general picture. Typically, in a given line-of-sight, the relative contribution of various dust components will vary. At the same time, the degree to which such variations can be detected and described is limited by the resolution and signal-to-noise ratios of the available data at the wavelengths involved. Thus, classifying populations of interstellar dust with common spectral parameters has been of high importance.

It was demonstrated by ? that a natural and highly effective classification of such populations can be achieved through the use of templates derived from surveys of spectral line emission (C II, H $\alpha$ , CO and H I) and from inference of nearby dust structures via starlight extinction (?). In this paper, we showed that using the linear minimization five such such templates, we can explain more than 95% of the signal variance at dust-dominated frequencies in *Planck* (353–857 GHz) and DIRBE (240–60  $\mu\text{m}$ ), and that it still accounted for more than 80% of the signal variance at the starlight-dominated DIRBE bands (25 and 12  $\mu\text{m}$ ).

? applied the main idea behind that result to all *Planck* HFI data using an extensive search of the full parameter space. It was shown that, by only using the *Gaia* extinction template, and by

assuming three other components with freely varying amplitudes per pixel, but with fixed global temperatures and spectral indices per component, we arrived at a dust model that could explain between 98.5% and 99.9% of the non-CMB signal in these channels. Furthermore, the resulting dust amplitude maps exhibited morphologies that turned out to be very similar to the templates used in ?, giving an independent confirmation of the appropriateness of assuming a morphological correlation between those astrophysical templates and dust populations.

Encouraged by these results, the main COSMOGLOBE DR2 analysis employs a similar four-component thermal dust model, in which four spatial templates are used to model the morphology of the thermal dust.

One of these templates, used in both ? and ?, was derived from the ? extinction maps (see ? for more details on how this template was constructed), while the three others were the best-fit solutions arrived at in ?. We plot these templates in Fig. ??.

The SEDs of these components are not directly modelled as modified blackbodies, as they were in ?. Rather, we define a set of SED bins, each of which is chosen to correspond to the width of a DIRBE band, as shown in ???. Each dust component is then set to be constant within a given bin, meaning that there is one free parameter per bin per component, which are then sampled over in the Gibbs chain.

With this, then, the total sky model (the third term of Eq. ??) in the frequency domain of DIRBE can be written,

$$\sum_{c=1}^{n_{\text{comp}}} \mathbf{M}_c(\nu) \mathbf{a}_c = [a]_{\text{cold}}(\nu) \mathbf{t}_{\text{cold}} \quad (\text{Cold dust}) \\ + [a]_{\text{hot}}(\nu) \mathbf{t}_{\text{hot}} \quad (\text{Hot dust}) \\ + [a]_{\text{nearby}}(\nu) \mathbf{t}_{\text{nearby}} \quad (\text{Nearby dust}) \\ + [a]_{H\alpha}(\nu) \mathbf{t}_{H\alpha} \quad (H\alpha \text{ correlated dust}) \\ + \left( \frac{\nu_{0,\text{ff}}}{\nu} \right)^2 \frac{g_{\text{ff}}(\nu; T_e)}{g_{\text{ff}}(\nu_{0,\text{ff}}; T_e)} \mathbf{t}_{\text{ff}} \quad (\text{Free-free}) \\ + U_{\text{mJy}} \sum_{j=1}^{n_s} f_{\text{Gaia},j} a_{s,j}, \quad (\text{Bright stars}) \\ + U_{\text{mJy}} f_{\text{Gaia},j} \mathbf{a}_{\text{fs},j}, \quad (\text{Faint stars}) \\ + m_\nu \quad (\text{Monopole}). \quad (5)$$

In this equation, the bracketed amplitudes,  $[a](\nu)$ , indicate amplitudes that are constant within each frequency range that corresponds to a DIRBE band (i.e. the abovementioned bins).

The first four terms form the complete model of thermal dust, which is the main focus of this work. The fifth term models the free-free emission, which is expected to contribute moderately at all relevant frequencies without becoming a dominant term. Then, there are two point source terms, all of which are dealt with in ?. Finally, the last term represents the monopole at each frequency, which is treated in ?.

### 3. Data

There are two datasets used directly in the COSMOGLOBE DR2 analysis: low-level data from COBE-DIRBE, and starlight data from WISE (?) and Gaia (??). They are supplemented by our dust templates, which are drawn from the analysis performed in ?, and incorporate data from Planck HFI and Gaia. Below we give a succinct description of these data sets and the preprocessing performed; for a more in-depth description, see ? and ?.

### 3.1. COBE-DIRBE

The Diffuse InfraRed Explorer (DIRBE), whose main goal was the mapping out of the cosmic infrared background (CIB), was part of the COBE satellite (??), and measured the sky in ten frequency bands from  $1\mu\text{m}$  to  $240\mu\text{m}$ . In this analysis, we have converted the original DIRBE CIO (Calibrated Individual Observations), whose pointing information is given in terms of Quadcube pixels with a resolution of  $20''$  into HEALPix  $N_{\text{side}}=512$  pixelation maps, giving an approximate resolution of  $42'$ . Following the nomenclature of ?, we refer to the DIRBE CIOs as “time-ordered data” (TOD). Including DIRBE TOD in the analysis in this way allows us to target the zodiacal light (?), which, as mentioned above, must be analysed as a time-varying component on the sky, in contrast to other astrophysical components.

The use of DIRBE data also allows a fuller exploration of the scales relevant for interstellar dust modelling; in particular, we are able to capture the “bump” and falling off of the thermal dust SEDs.

### 3.2. WISE and Gaia

At the higher DIRBE frequency bands ( $25\text{--}125\mu\text{m}$ ), starlight emission becomes a significant source of emission, both as point sources and as a diffuse component. Using the AllWISE pointsource catalog (?), we crossmatched the brightest stars in the W1 band against Gaia DR2, and used the estimated physical parameters from that catalogue to model the bright stars. In addition, we created a general “faint source” template based on the stars that were not part of the bright star component. Together, these two components comprise the sixth and seventh component in ??.

### 3.3. Data selection

As noted in ?, not all thermal dust components are expected to contribute to the DIRBE bands we are considering in this paper (i.e.  $240\text{--}12\mu\text{m}$ ). Following the same logic as in that paper, we restrict the dust components to be active in the various DIRBE bands as indicated in Table ???. NEED EXPLANATION HERE.

### 3.4. Masks

As discussed in ?...

## 4. Results

The analysis consisted of five Gibbs chains, each of which contained approximately 250 samples. Out of these, in what follows (except for the traceplots), the first 100 samples are considered the burn-in period, since (as explained below) all chains seem to have converged by then.

### 4.1. Markov chains, correlations and convergence

In ????????, we plot the Gibbs chain traceplots for all the five Gibbs chains used in the analysis, for all four dust components. After a period of reaching equilibrium – which varies from almost instantly (for the cold dust amplitude, for example) to around 100 samples at the most (particularly evident for the hot dust and  $H\alpha$ -correlated dust  $25$  and  $12\mu\text{m}$  bins) – the chains generally do not exhibit any long correlations and seem to mix fairly well. The only exception is the  $240$  and  $120\mu\text{m}$   $H\alpha$ -correlated

**Table 1.** Components enabled for each frequency band. Band widths correspond to the width of the corresponding dust band used in this analysis, not the instrumental bandwidths.

Band	Dust Band Width (GHz)	Hot dust	Cold dust	Nearby dust	H $\alpha$ -correlated dust
DIRBE 240 $\mu\text{m}$	617	x	x	x	x
DIRBE 140 $\mu\text{m}$	873	x		x	x
DIRBE 100 $\mu\text{m}$	1524	x		x	x
DIRBE 60 $\mu\text{m}$	4936	x		x	x
DIRBE 25 $\mu\text{m}$	9100	x		x	x
DIRBE 12 $\mu\text{m}$	27400	x		x	x
DIRBE 4.9 $\mu\text{m}$	24715	x			
DIRBE 3.5 $\mu\text{m}$	39275	x			

dust bins, where we see more long-term trends that indicate a slower traversal through parameter space.

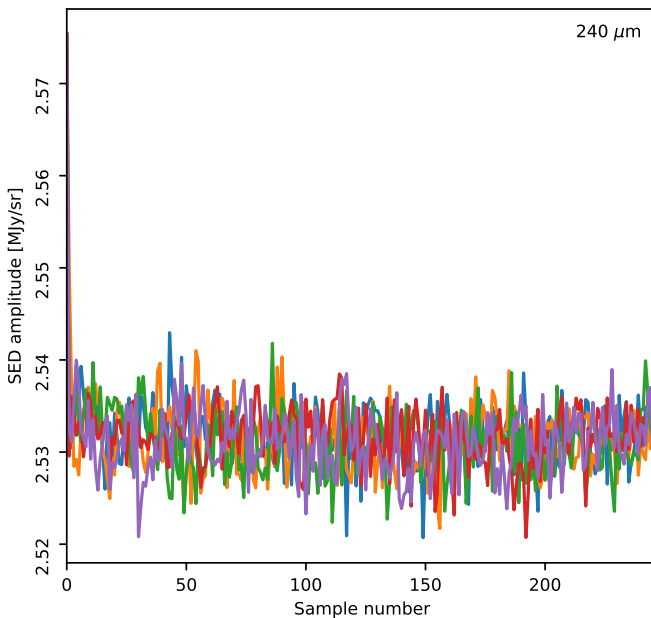


**Fig. 2.** Cold dust amplitude as a function of iteration for the 240  $\mu\text{m}$  channel where it is included. The five lines correspond to the five independent sampling chains in the analysis. We see robust mixing in all chains.

In Fig. ??, we show the correlations between the various SED bins in the run, calculated over all five chains after discarding burn-in. The strongest correlations are internally between the near dust bins. Most of them are correlated with each other, but they are anticorrelated with the 12  $\mu\text{m}$  amplitude. Those same bins, and in particular the 100  $\mu\text{m}$  one, are also anticorrelated with the 100  $\mu\text{m}$  hot dust amplitude. It seems reasonable enough, looking at Fig. ??, that there is overlap between the components, and as long as the morphologies of hot dust and nearby dust are similar enough that whenever the one increases, the other can decrease to compensate for the change. The same phenomenon can be seen between hot and cold dust at 240  $\mu\text{m}$ .

#### 4.2. Multi-component thermal dust SED posteriors

In Table ??, we summarize the thermal dust SED posteriors resulting from the above analysis as the mean value and variance of the chain samples (including all five chains of the analysis, discarding burn-in). Similarly, we plot the posterior mean values

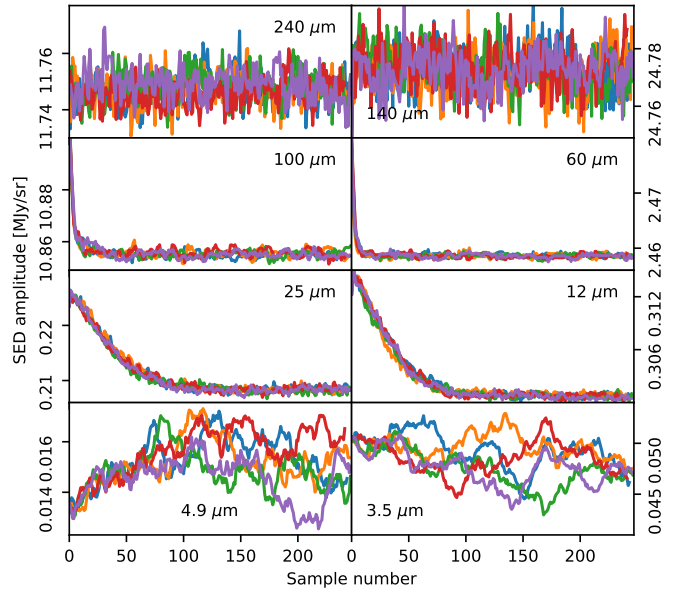


**Fig. 3.** Hot dust amplitudes as a function of iteration for the eight lowest frequency DIRBE channels, with all five sampling chains overplotted. We see that the 3.5  $\mu\text{m}$  and 4.9  $\mu\text{m}$  channels exhibit slower mixing than the others, but still manage to explore the full parameter space.

per bin in Fig. ??, where the thickness of the line indicates the standard deviation of that amplitude.

In the same plot, we also plot posterior total SED, when all four components are summed up, and we also show the Astro-dust+PAH model that is the best fit to the mean total dust SED.<sup>5</sup>

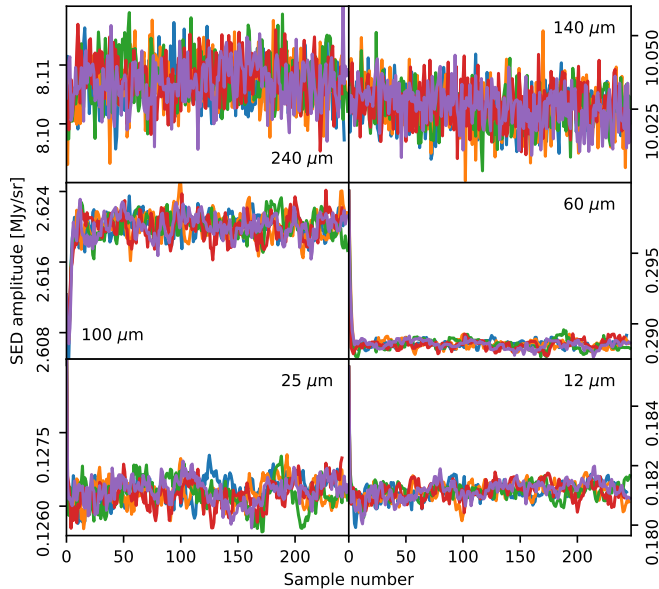
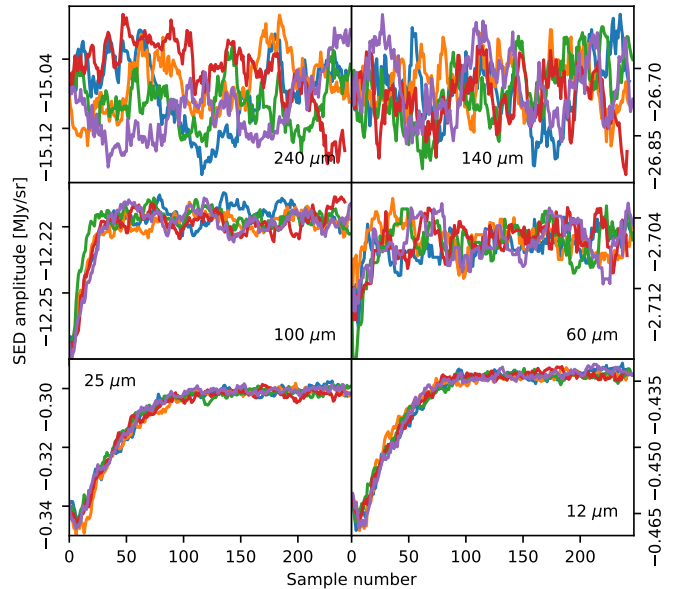
Clearly, both the hot dust and nearby dust components follow a typical thermal dust modified blackbody curve, mirroring the results found in ?. At higher frequencies, we also see that they exhibit the characteristic rise in the SED, where models like Astro-dust+PAH predicts emission lines from the nanoscale particles. The figure also shows that fitting the total (i.e. the sum of all the components) dust model to the Astro-dust+PAH model yields a version of the latter that seems to fit very well with the posterior mean SED values.

We cannot draw any such conclusions about the the cold dust component, as it is only active for the lowest SED bin; in any case, the hot dust component clearly dominates this bin.

<sup>5</sup> Specifically, we fit an overall amplitude  $A$ , as well as the  $\log_{10} U$  parameter used in ?, with the total model to fit being  $A \cdot \text{EM}(\log_{10} U)$ , where  $\text{EM}$  is their tabulated function returning the emission as a function of  $\log_{10} U$ .

**Table 2.** Summary of dust template amplitude posterior constraints.

$\lambda$ ( $\mu\text{m}$ )	BAND (THz)		TEMPLATE AMPLITUDE (UNIT)			
	$\nu_{\min}$	$\nu_{\max}$	$a_h$	$a_c$	$a_n$	$a_{H\alpha}$
3.5 . . . . .	70.2	109.5	$0.05 \pm 0.00$	$0.00 \pm 0.01$	$0.01 \pm 0.00$	$0.00 \pm 0.01$
4.9 . . . . .	45.5	70.2	$0.01 \pm 0.00$	$0.00 \pm 0.01$	$0.01 \pm 0.00$	$0.00 \pm 0.01$
12 . . . . .	18.1	45.5	$0.30 \pm 0.00$	$0.00 \pm 0.01$	$0.19 \pm 0.00$	$-0.32 \pm 0.01$
25 . . . . .	9.0	18.1	$0.22 \pm 0.00$	$0.00 \pm 0.01$	$0.13 \pm 0.00$	$-0.28 \pm 0.01$
60 . . . . .	4.1	9.0	$2.45 \pm 0.00$	$0.00 \pm 0.01$	$0.31 \pm 0.00$	$-2.41 \pm 0.03$
100 . . . . .	2.5	4.1	$10.92 \pm 0.03$	$0.00 \pm 0.01$	$2.61 \pm 0.00$	$-12.40 \pm 0.02$
140 . . . . .	1.7	2.5	$24.58 \pm 0.01$	$0.00 \pm 0.01$	$10.04 \pm 0.01$	$-23.40 \pm 0.08$
240 . . . . .	1.1	1.7	$11.33 \pm 0.01$	$2.60 \pm 0.01$	$8.09 \pm 0.01$	$-8.94 \pm 0.04$

**Fig. 4.** Nearby dust amplitudes as a function of the iteration for the six lowest frequency DIRBE channels, with all five sampling chains overplotted. We see robust mixing in all chains and for all frequency channels.**Fig. 5.**  $H\alpha$  dust amplitudes as a function of the iteration for the six lowest frequency DIRBE channels, with all five sampling chains overplotted. We see that the 25 and 12  $\mu\text{m}$  channels exhibit slower mixing than the others, but still manage to explore the full parameter space.

The  $H\alpha$  component, as in the previous analyses, exhibits a negative SED, and is thus responsible for dust extinction rather than emission, but it exhibits the same blackbody spectrum with a hint of a rise towards the PAH emission region.

#### 4.3. Model efficiency and residuals

In ??, we show the dust frequency maps – that is, the frequency maps with starlight and free-free signal subtracted – as well as the residual maps after subtracting the four-component dust model used in this analysis. The grey pixels indicate the masks used at each frequency, as described in ???. In all the bands to some degree, we see in the residuals a weak pattern of over-and-undersubtractions in the galactic plane, suggesting that there is room for further sophistication of the template model. At the higher frequencies, the model is clearly struggling to account for emission from the galactic center.

IS THE EFFICIENCY FIGURE ACCURATE? ??

## 5. COSMOGLOBE DR2 sky model

### 5.1. Summary of global sky model

In Fig. ?? we show the best-fit COSMOGLOBE sky model, derived from the first and second data releases, including the four-component dust model presented in this paper. Although the amplitudes chosen are relatively arbitrary (every line of sight in the sky will potentially have different scalings), the spectral shape of the lines are directly taken from the Gibbs chains as presented in ? and ?. This plot represents the current state of the Cosmoglobe effort to create a common sky model derived with the same data pipeline.

Finally, in ??, we show the amplitude maps of all the components involved in the COSMOGLOBE DR2 analysis, including zodiacal light, dust, starlight, and free-free emission. These maps represent the Cosmoglobe sky model as applied to the DIRBE bands, and in the final column we see the residual maps at each band. At the two lowest bands, where the thermal dust is the dominant sky component (see Fig. ??), the model is performing quite well (with the same caveats as for the pure dust residual maps), especially given that we essentially treat the thermal dust

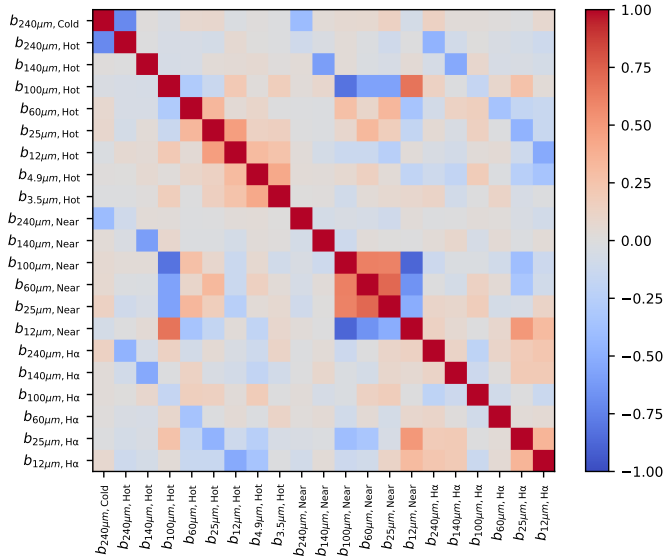


**Fig. 6.** Correlations between the dust amplitudes at each frequency, as computed over the full sample set. We see that they are largely uncorrelated, but we see some structures within some bands as the sampler trades off between components (eg.  $240\mu\text{m}$  in the upper left). We also see some fainter structure in the nearby dust amplitudes across channels.

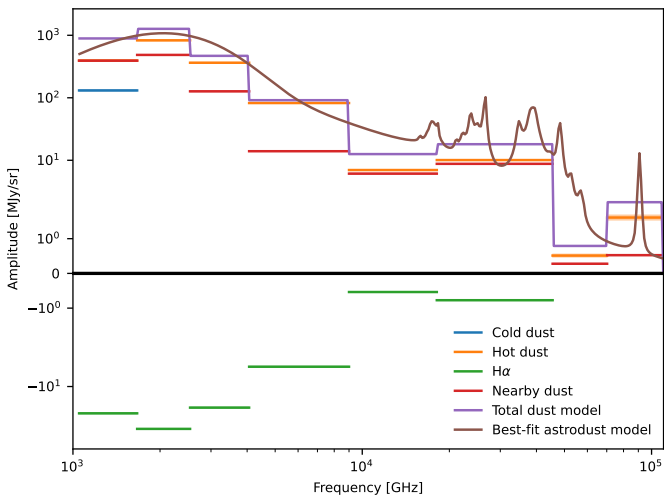


**Fig. 7.** The total dust SED as a function of frequency, as well as the four dust components. The best-fit astrodust model fit to the total SED for the frequencies shown is also plotted in brown.

as a model with  $\sim 20$  free parameters, instead of fitting two spectral parameters per pixel on the sky.

At higher frequencies, the model struggles more (as also seen in Figs. ?? and ??). There is clearly residual zodiacal light at the intermediate frequencies, whereas at the highest frequencies we see there is residual starlight in the maps (evident also in Fig. ??), where band 2, which is the one where the starlight SED peaks, is where the sky model currently performs the worst.

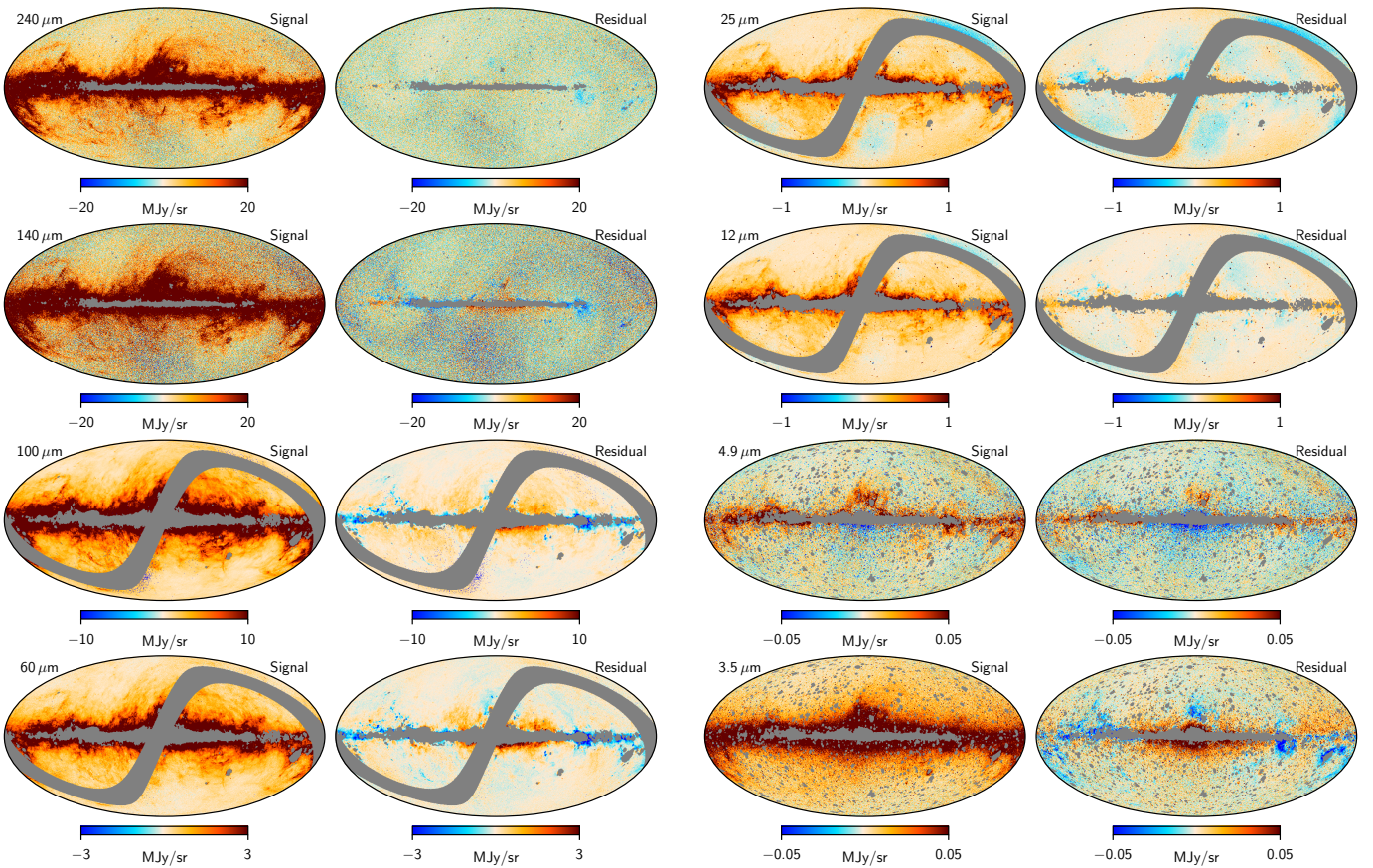


**Fig. 8.** Comparison between thermal dust frequency maps (i.e., stationary sky signal minus starlight and free-free; *first and third columns*) and residual maps for each frequency channel (*second and fourth column*). Gray pixels indicate the analysis masks used for each frequency channel.

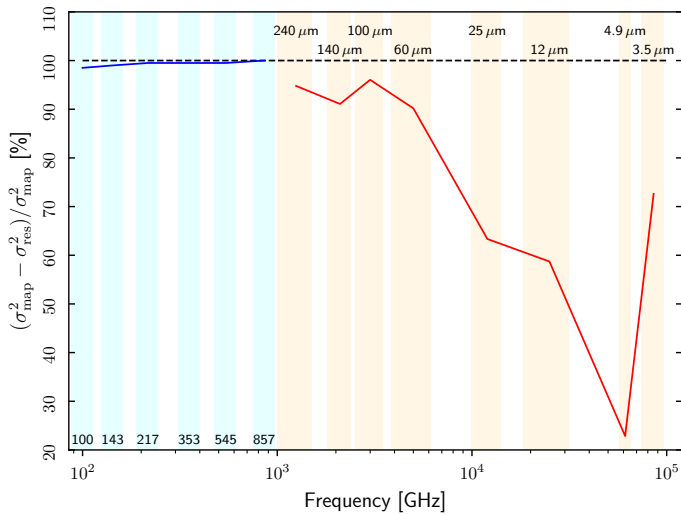


**Fig. 9.** Dust model efficiency as a function of frequency, as defined in terms of variance reduction. The red line shows results for DIRBE, as evaluated from the maps shown in Fig. ??, while the blue line shows results for *Planck* HFI, as presented by ?. Vertical bands indicate the position and bandwidth of each DIRBE (orange) and HFI (cyan) frequency channel.

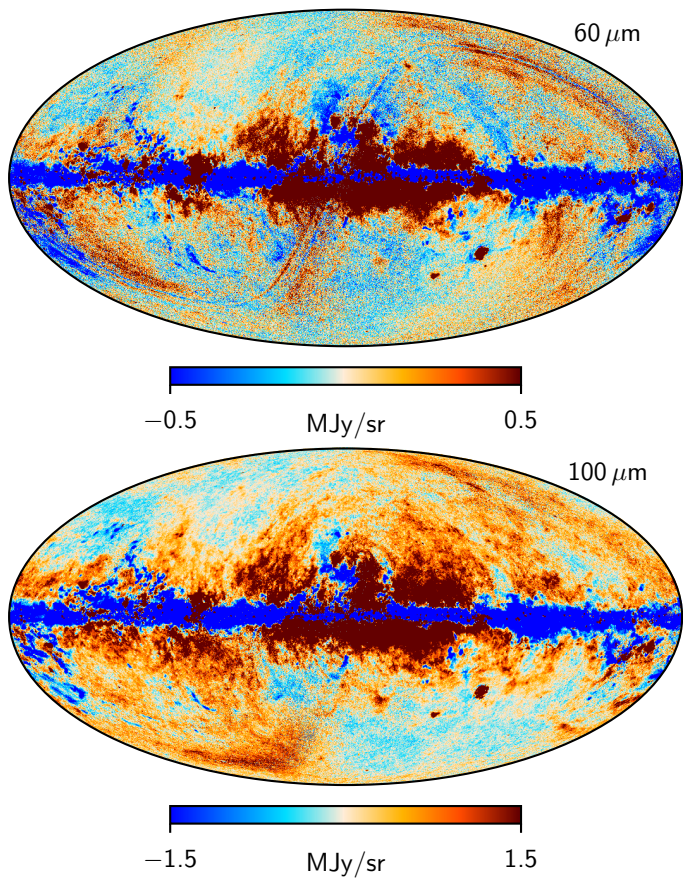


**Fig. 10.** Full-sky data-minus-model residual maps for the 60 (top) and 100  $\mu\text{m}$  (bottom) DIRBE channels.

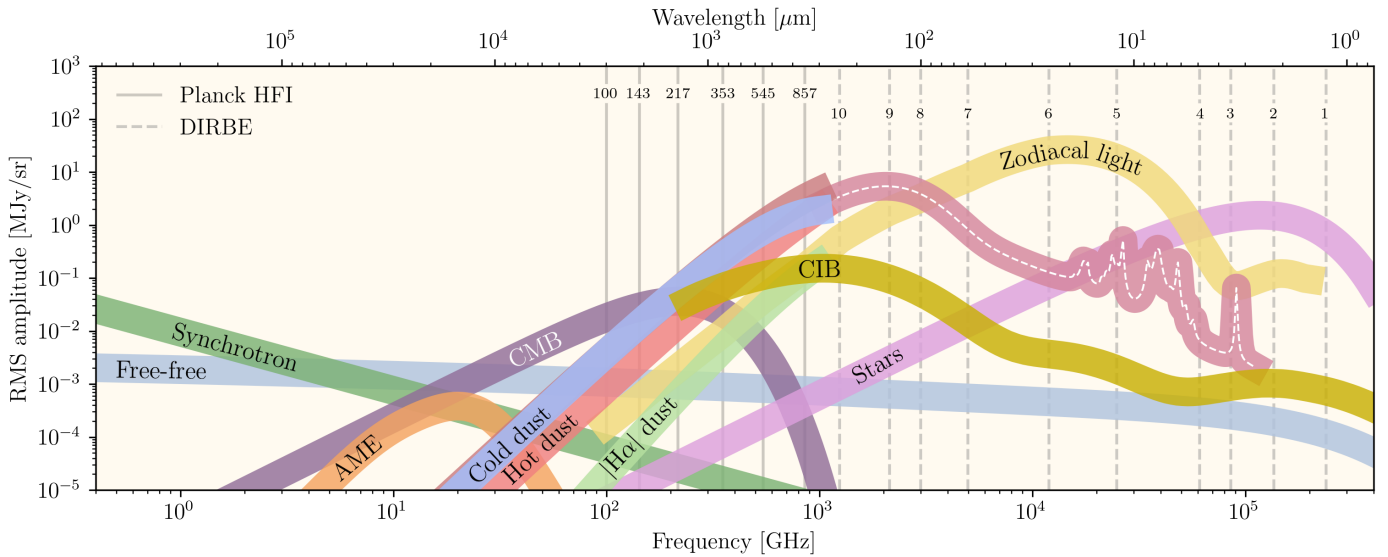


**Fig. 11.** Overview of the large-scale microwave and infrared sky from 1 GHz to  $1\mu\text{m}$ , based on the COSMOGLOBE DR1 and DR2 data. The four component dust model is shown, as well as the best fit astrodust model. The *Planck* HFI and DIRBE central frequencies are indicated with vertical lines.

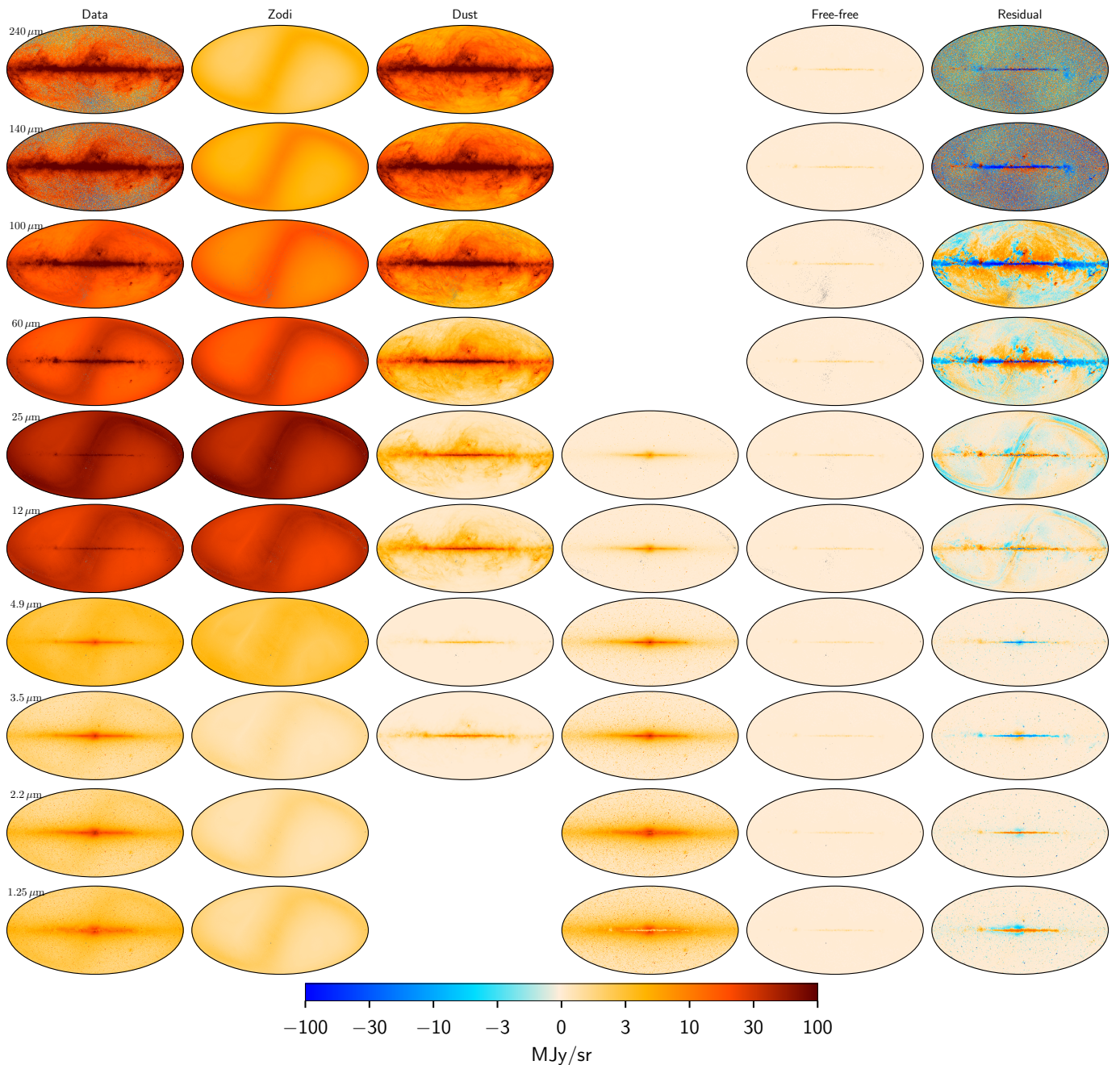


**Fig. 12.** Comparison between the re-analyzed DIRBE data and the various fitted components for one single Gibbs sample. Columns show, from left to right, 1) the time-ordered DIRBE data co-added into pixelized maps; 2) zodiacal light emission; 3) thermal dust emission; 4) star emission; 5) free-free emission; and 6) data-minus-model residual emission. Rows show individual frequency channels. Missing entries corresponds to components that are forced to zero in the model. Note that all panels are plotted with the same color scale in units of MJy/sr, and can be directly compared. **MG: stars needs a label**

## 6. Conclusions

In this analysis, which is part of the second COSMOGLOBE data release, we have described the incorporation of a four-component model, presented in ?, as part of the modelling of thermal dust at the eight lowest DIRBE frequency bands. Recent analyses (??) demonstrated the feasibility and efficiency of decomposing thermal dust into a relatively low number of distinct populations with global spectral parameters.

The model uses a nearby dust template presented in ?, labeled “nearby dust”, as well as the three template components derived in ?, labeled “Hot dust”, “Cold dust”, and “H $\alpha$ -correlated dust”, respectively. The SED of each component was defined as a constant bin over each DIRBE band.

With this model as part of the larger DR2 analysis, we showed that the resulting total SED is an excellent match to the AstroDust+PAH model, and that the nanoparticle emission at high frequencies is detected in these components. As in previous analyses, the H $\alpha$ -correlated component absorbs rather than emits radiation, and thus has a negative SED.

Finally, we present the current state of the COSMOGLOBE sky model, ranging from a few GHz to  $10^3$  THz, and containing diverse components, such as the CMB, synchrotron radiation, zodiacal light, starlight, the various thermal dust components, and the CIB.

Although the results in this and the preceding analyses are very encouraging for the prospect of efficient thermal dust modelling, it is clearly also something that is in need of further development..... Also, this analysis only utilizes one data set in addition to the starlight data. An obvious extension would be to perform a joint analysis ranging across the entirety of the thermal dust spectrum, with higher-resolution data both in the spatial domain and in the frequency domain.

A promising combination of data, which is definitely within the realm of possibility in a joint analysis framework such as COSMOGLOBE, could be as follows: 1) *Planck* low-level data for the low end of the thermal dust spectrum, and correlation with various types of line emission; 2) DIRBE, as in the present analysis, to constrain the upper part of the thermal dust spectrum, including the PAH features; 3) AKARI (?), observing in the same range as DIRBE, but with higher resolution, thus shedding light on an otherwise data-poor part of the electromagnetic spectrum; and 4) *IRAS*, to provide ....

**Acknowledgements.** The current work has received funding from the European Union’s Horizon 2020 research and innovation programme under grant agreement numbers 819478 (ERC; COSMOGLOBE) and 772253 (ERC; birs2cosmology). Some of the results in this paper have been derived using the HEALPix (?) package. We acknowledge the use of the Legacy Archive for Microwave Background Data Analysis (LAMBDA), part of the High Energy Astrophysics Science Archive Center (HEASARC). HEASARC/LAMBDA is a service of the Astrophysics Science Division at the NASA Goddard Space Flight Center. This paper and related research have been conducted during and with the support of the Italian national inter-university PhD programme in Space Science and Technology. Work on this article was produced while attending the PhD program in PhD in Space Science and Technology at the University of Trento, Cycle XXXIX, with the support of a scholarship financed by the Ministerial Decree no. 118 of 2nd March 2023, based on the NRRP - funded by the European Union - NextGenerationEU - Mission 4 "Education and Research", Component 1 "Enhancement of the offer of educational services: from nurseries to universities" - Investment 4.1 "Extension of the number of research doctorates and innovative doctorates for public administration and cultural heritage" - CUP E66E23000110001.

- Ade, P. A. R., Ahmed, Z., Amiri, M., et al. 2021, Phys. Rev. Lett., 127, 151301  
 Boggess, N. W., Mather, J. C., Weiss, R., et al. 1992, ApJ, 397, 420  
 Edenhofer, G., Zucker, C., Frank, P., et al. 2024, A&A, 685, A82  
 Eisenhardt, P. R. M., Marocco, F., Fowler, J. W., et al. 2020, ApJS, 247, 69  
 Eriksen, H. K., O’Dwyer, I. J., Jewell, J. B., et al. 2004, ApJS, 155, 227  
 Gaia Collaboration et al. 2016, A&A, 595, A1  
 Gaia Collaboration et al. 2018, A&A, 616, A1  
 Galloway, M., Andersen, K. J., Aurién, R., et al. 2023, A&A, 675, A3  
 Galloway, M. et al. 2026, A&A, in preparation [arXiv:20xx.xxxxx]  
 Geman, S. & Geman, D. 1984, IEEE Trans. Pattern Anal. Mach. Intell., 6, 721  
 Gjerløw et al. 2026, A&A, in preparation [arXiv:20xx.xxxxx]  
 Górski, K. M., Hivon, E., Banday, A. J., et al. 2005, ApJ, 622, 759  
 Hauser, M. G., Arendt, R. G., Kelsall, T., et al. 1998, ApJ, 508, 25  
 Hensley, B. S. & Draine, B. T. 2021, ApJ, 906, 73  
 Hensley, B. S. & Draine, B. T. 2023, ApJ, 948, 55  
 Kelsall, T., Weiland, J. L., Franz, B. A., et al. 1998, ApJ, 508, 44  
 LiteBIRD Collaboration, Ally, E., Arnold, K., et al. 2023, Progress of Theoretical and Experimental Physics, 2023, 042F01  
 Murakami, H., Baba, H., Barthel, P., et al. 2007, PASJ, 59, S369  
 Planck Collaboration XI. 2014, A&A, 571, A11  
 Planck Collaboration X. 2016, A&A, 594, A10  
 Planck Collaboration III. 2020, A&A, 641, A3  
 Planck Collaboration XI. 2020, A&A, 641, A11  
 Planck Collaboration XII. 2020, A&A, 641, A12  
 Planck Collaboration Int. XIV. 2014, A&A, 564, A45  
 Planck Collaboration Int. XVII. 2014, A&A, 566, A55  
 Planck Collaboration Int. XIX. 2015, A&A, 576, A104  
 Planck Collaboration Int. XXII. 2015, A&A, 576, A107  
 Planck Collaboration LVII. 2020, A&A, 643, A42  
 Popovic, B., Shah, P., Kenworthy, W. D., et al. 2025, arXiv e-prints, arXiv:2511.07517  
 San, M. et al. 2024, A&A, in preparation [arXiv:20xx.xxxxx]  
 Seljebotn, D. S., Bærlund, T., Eriksen, H. K., Mardal, K. A., & Wehus, I. K. 2019, A&A, 627, A98  
 Silverberg, R. F., Hauser, M. G., Boggess, N. W., et al. 1993, in Society of Photo-Optical Instrumentation Engineers (SPIE) Conference Series, Vol. 1919, Infrared Spaceborne Remote Sensing, ed. M. S. Scholl, 180–189  
 Sullivan et al. 2026, A&A, in preparation [arXiv:20xx.xxxxx]  
 Thorne, B., Dunkley, J., Alonso, D., & Næss, S. 2017, MNRAS, 469, 2821  
 Watts, D., Galloway, M., Gjerløw, E., et al. 2024a, A&A, submitted [arXiv:2408.10952]  
 Watts, D. et al. 2024b, A&A, in preparation [arXiv:2406.01491]  
 Watts, D. J., Basyrov, A., Eskilt, J. R., et al. 2023, A&A, 679, A143  
 Wright, E. L., Eisenhardt, P. R. M., Mainzer, A. K., et al. 2010, AJ, 140, 1868  
 Zonca, A., Singer, L., Lenz, D., et al. 2019, Journal of Open Source Software, 4, 1298  
 Zonca, A., Thorne, B., Krachmalnicoff, N., & Borrill, J. 2021, Journal of Open Source Software, 6, 3783

## References

- Ade, P., Aguirre, J., Ahmed, Z., et al. 2019, J. Cosmology Astropart. Phys., 2019, 056